Lasers in Manufacturing Conference 2025

Influence of particle size distribution and drying states on laser beam melting of lunar regolith simulants

T. Eismann[a], T. Griemsmann[a], M. Ernst[a], J. Duesing[a], M. Springer[a], P. Dyroey[a], R. Kalms[a], M. Müller[a], P. Wessels[a], J. Neumann[a], N. Schwarz[a], B. Grefen[b], S. Linke[b], E. Stoll[b], S. Kaierle[a,c]

[a] *Laser Zentrum Hannover e.V., Hollerithallee 8, 30419 Hannover, Germany*
[b] *Technische Universität Berlin, Marchstraße 12 - 14, 10587 Berlin, Germany*
[c] *Institut für Transport- und Automatisierungstechnik, Leibniz Universität Hannover, An der Universität 2, 30823 Garbsen, Germany*

Abstract

The Moon serves as a stepping stone for humanity's space colonization. Due to high transportation costs, utilizing lunar resources is considered essential for further development in space applications. Lunar regolith and its simulants exhibit a wide range of particle size distributions (PSDs). Simulants prepared under terrestrial conditions retain moisture, requiring pre-drying. Within this work, the influence of these characteristics on the melting process similar to a powder bed fusion process has been investigated.
Simulant powders with different PSDs (particle sizes $\leqslant$ 1000 µm) and drying states (undried, 300 °C and 800 °C for 4 h) were processed in a vacuum chamber and the fabricated specimens profoundly analyzed. The results show an increase in specimen mass with larger particles and higher drying temperatures. No correlation of the PSD and drying temperature on the porosity was observed. Processing of undried simulants caused the formation of discontinuous melt tracks and a significant chamber pressure increase.

Keywords: In situ resource utilization, Laser beam melting, Regolith melting, Regolith

1. Introduction

The Moon serves as a crucial stepping stone for future human space exploration, particularly as a testing ground for technologies geared toward Mars and beyond. Due to the very high costs of transporting materials from Earth, efficient in situ resource utilization (ISRU) of lunar materials is vital for sustainable missions (Sacksteder and Sanders 2007). Lunar regolith, a fine-grained and mineralogically complex soil covering the Moon's surface, offers a plentiful raw material for manufacturing infrastructure such as landing pads, pathways, and habitats (Heiken et al. 1991; Isachenkov et al. 2021; Gerdes et al. 2018). The regolith is composed of a variety of mineral oxides, with silicon oxide as the predominant constituent (Jolliff et al. 2006). Owing to its chemical composition, it is well suited for melting-based processing methods and therefore represents a promising resource for additive manufacturing applications (Fateri and Gebhardt 2015; Gerdes et al. 2018).

In 2012, Balla et al. reported that the lunar regolith simulant JSC-1AC could be processed using laser cladding, enabling the production of dense structures (Krishna Balla et al. 2012). Building on this, Fateri et al. demonstrated the feasibility of processing JSC-1A simulant into three-dimensional parts using powder bed fusion with a laser beam (PBF-LB) (Fateri and Gebhardt 2015; Fateri et al. 2013). The experiments were performed at atmospheric pressure, and particles larger than 200 µm were removed by sieving prior to processing. In 2018, researchers from the Laser Zentrum Hannover (LZH) and the Institute of Space Systems at TU Braunschweig (IRAS) successfully processed a basalt-based regolith simulant on a commercial PBF-LB system under argon atmosphere (Gerdes et al. 2018). Similarly, Caprio et al. employed the regolith simulant NU-LHT-2M to fabricate mechanically stable single-layer components using PBF-LB technology (Caprio et al. 2020).

All these approaches involved adaptations with respect to actual lunar conditions to enable the processing of regolith simulants. These included processing under ambient atmospheric pressure, particle size selection through sieving, and the use of solid substrates to facilitate heat dissipation. In contrast, researchers from LZH developed a process, as part of the Moonrise project, that is expected to operate under real lunar environmental conditions on the Moon's surface, without

requiring further adaptation (Neumann et al. 2023). To validate this approach, melting experiments were conducted in loosely packed powder beds under vacuum (Eismann et al. 2023; Eismann et al. 2024; Griemsmann et al. 2024; Griemsmann et al. 2025), and even the influence of lunar gravity was investigated (Reitz et al. 2021; Overmeyer et al. 2025).

Despite differences in process design and environmental boundary conditions, all studies consistently demonstrate the fundamental feasibility of laser beam melting of lunar regolith simulants. However, substantial research gaps remain concerning the influence of specific material properties on process behavior and outcome. Both the experimental environments used in prior work and the simulants themselves differ significantly among each other as well as from actual lunar conditions. This contribution focuses on two key differences between terrestrial simulants and lunar regolith and investigates their impact on the laser beam melting process.

First, it is important to note that terrestrial regolith simulants generally contain water of crystallization and small amounts of free water. In addition, moisture is introduced during the synthesis process and through exposure to ambient atmospheric conditions during storage and handling. Conversely, lunar regolith, except for trace amounts, is essentially anhydrous (Heiken et al. 1991). The presence of moisture and water of crystallization in simulants is considered undesirable (Slabic et al. 2024), as it is suspected to contribute to process issues such as pore formation, gas inclusions, and uncontrolled spattering during melting (Eismann et al. 2023). Therefore, the aim of the first study presented in this contribution is to quantify the influence of moisture and water of crystallization on the process behavior and the produced specimens, and to determine to what extent thermal desiccation (also referred to as drying state) is necessary to ensure a stable and reproducible laser beam melting process. To address this, three drying states are compared: untreated powder (containing both free and bound water), powder dried at 300 °C for four hours (to remove free moisture), and powder dried at 800 °C for four hours (to additionally remove water of crystallization).

Secondly, the particle size distribution (PSD) of the regolith feedstock plays a critical role in powder-based laser melting processes (Popovich et al. 2020). The central objective of the second study was therefore to quantify this influence on laser melting of regolith and to determine the most favorable PSD ranges for future in situ lunar processing. Lunar regolith naturally spans a wide PSD range, from sub-micron dust to millimeter-scale fragments, depending on location, depth, and geological history. In PBF-LB, the PSD significantly influences powder bed packing density, laser absorption characteristics, melt pool dynamics, and thermal conductivity within the melt and surrounding material (Averardi et al. 2020; Zhang et al. 2019; Gusarov and Kovalev 2009). In the second study, three distinct PSD fractions were selected (0–90 µm, 160–250 µm, and 500–1000 µm) to investigate their respective effects on the laser beam melting process behavior.

2. Material and Methods

2.1. Experimental materials

The lunar base simulant TUBS-T, which was produced by TU Berlin, was used for both studies. For the experiments on the influence of drying states, the base simulant TUBS-M and a so-called South Pole Simulant were also used. The South Pole Simulant is a mixture of 90% TUBS-T and 10% TUBS-M. The chemical composition of the TUBS-T and -M simulant is given in Table 1 (based on (Linke 2022)).

The particles of the regolith simulants are sharp-edged as shown in Figure 1 and exhibit a particle size below 2 mm. For the experiments on the influence of the particle size distribution, the powder was sieved, resulting in three size distributions, as shown in Table 3 Section 2.3.

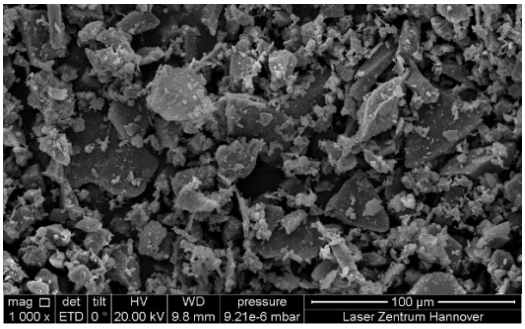

Figure 1. SEM image of South Pole Simulant (dried at 800 °C for four hours)

Table 1. Composition of regolith simulants in wt.-% (based on (Linke et al. 2020))

Oxide	SiO_2	TiO_2	Al_2O_3	FeO	MgO	CaO	Na_2O	K_2O	MnO	Cr_2O_3	P_2O_5
TUBS-M	48.61	2.29	13.28	10.14	8.73	8.31	3.67	1.71	0.18	0.04	0.51
TUBS-T	48.71	0.12	30.33	1.05	0.57	14.57	3.05	0.22	0.02	0	0

2.2. Experimental equipment

The experimental setup utilized for the laser beam melting process is illustrated in Figure 2 (a). A diode laser system that provides a maximum optical output power of 140 W at a wavelength around 976 nm was used as the beam source. During the experiments, the system was operated at a working distance around 230 mm, resulting in a measured laser spot diameter of approximately 2 mm. The system was mounted on a motorized gantry system.

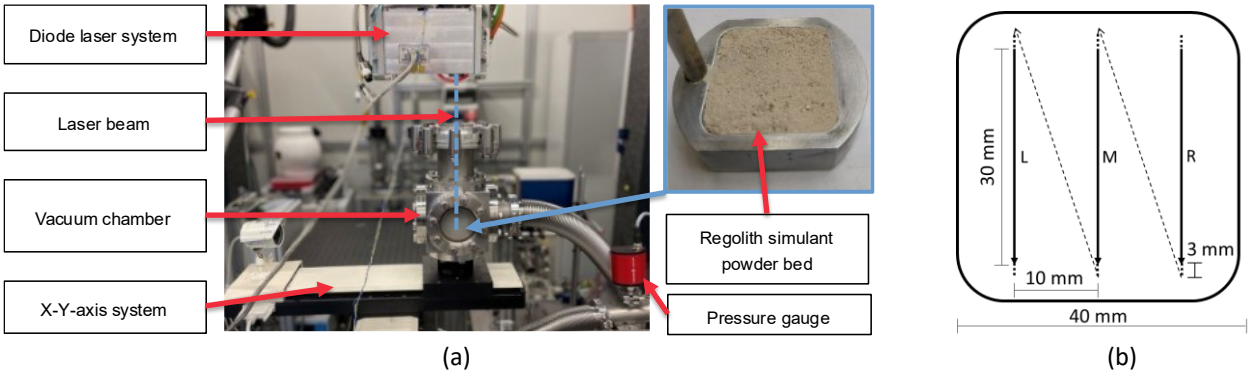

Figure 2. (a) Experimental setup with a powder bed of TUBS-M and (b) Processing scheme for the laser melting experiments, i.e. relative movement between chamber and laser system (solid line = laser on; dashed line = laser off)

Below the laser a vacuum chamber was placed on a linear axis system. It was connected to a vacuum pump stand (TSH 071 E, Pfeiffer Vacuum GmbH). The vacuum chamber contained a removable aluminum powder tray with a base area of 39 x 40 mm (corresponds to the X-Y plane within the scope of this paper) and a depth of 8 mm (corresponds to the Z plane within the scope of this paper). The powder tray is filled with regolith simulants to create a powder bed. The relative movement speed between the laser and the vacuum chamber remained at 1 mm/s throughout all experiments.

2.3. Experimental methods

The experimental procedure was consistent across both studies. A powder bed was prepared and placed inside the vacuum chamber. Subsequently, an initial target pressure of approximately 1.5×10^{-2} mbar was generated. This pressure corresponds to the lowest pressure that could be repeatedly generated with dry simulant powder. However, in some experiments from the study regarding the drying state, this target pressure could not be achieved (see Figure 5 in Section 3.1). Following evacuation, the operation of the pump was stopped and the powder bed was selectively molten to fabricate three specimens. The manufacturing of three specimens in one powder bed is referred to as one run. Upon completion, the powder bed containing the specimens was removed from the chamber and replaced with a fresh powder bed. This cycle was then repeated.

Each specimen was fabricated with a nominal length of 30 mm, as illustrated in Figure 2 (b). The scan vectors, shown as solid lines, indicate the paths of laser exposure. Since the operator must manually start the laser exposure, the relative movement between the laser and the chamber begins and ends 3 mm before and after the scan vectors, respectively. This can be seen from the dashed lines in Figure 2 (b). This ensures a constant scan speed throughout the entire exposure period. After completing each scan vector, the laser is repositioned to the start of the next vector. The spacing between adjacent scan vectors was maintained at 10 mm.

Table 2 summarizes the process parameter settings and powder characteristics used in the study investigating the influence of drying states. The simulants utilized were TUBS-M, TUBS-T, and the South Pole simulant. For each simulant, powder batches of approximately 50 g were dried at 300 °C and 800 °C for 4 hours under atmospheric pressure. Additionally, undried powder was used as a reference.

The used laser power ranged from 89 to 97 W. This fluctuation could not be prevented for technical reasons but does not significantly affect the process. For undried powder, only three specimens were produced per simulant due to significant contamination of the upper laser entry window of the vacuum chamber during these runs. A similar limitation applied to tests with powder dried at 300 °C, although six specimens were successfully fabricated for TUBS-M and the South Pole simulant. For powders dried at 800 °C, three runs per simulant were completed, resulting in a total of nine specimens.

Table 2. Process parameter settings and simulant powder conditions for the study regarding the influence of the drying states

Simulant	Drying states/temperatures	Laser beam power	Number of specimens
TUBS-M	Undried, 300 °C, 800 °C	89 W	3 (undried), 6 (300 °C), 9 (800 °C)
TUBS-T	(Drying for 4 h under atmosphere)	89 – 97 W	3 (undried), 3 (300 °C), 9 (800 °C)
South Pole		89 – 97 W	3 (undried), 6 (300 °C), 9 (800 °C)

The process parameter settings for the study on the influence of the PSD are given in Table 3. For the < 90 µm fraction, only one run consisting of three specimens was performed due to the mentioned issue regarding the entry window. For the other two PSDs, three runs were conducted for each, resulting in a total of nine specimens per PSD. Prior to processing, all powders were thermally treated by drying at 800 °C for four hours under atmospheric conditions.

Table 3. Process parameter settings and simulant powder conditions for the study regarding the influence of the PSD

Simulant	PSD in µm	Laser beam power	Number of specimens
TUBS-T	< 90	89 W	6
	160 - 250		9
	500 - 1000		9

2.4. Methods for analysis

After the specimens were removed from the powder bed, any adhering particles were brushed off. The specimens were then weighed on a Sartorius AG BP 3100 S. It should be noted that this procedure only applied to specimens that could be completely recovered from the powder bed. Some specimens consisted of multiple non-cohesive melt beads, that could not be clearly assigned to a specific sample. These specimens weren't weighed. The specimens of the PSD study were then photographed in the X-Y plane and their width and length were determined based on the images.

To determine the porosity of the specimens, cross-sections were prepared in the Y–Z plane and photographed using a laser scanning microscope (VKX 1000, Keyence). The resulting micrographs were processed using a Python-based image analysis workflow. Initially, the background was removed by identifying a representative background color from a selected region in the image corner and excluding all connected pixels of similar color from further analysis. This step ensures that only the specimen area is evaluated. Following background removal, the image was converted to grayscale, and a thresholding method was applied to distinguish between dense material and pores. Pixels above the threshold were classified as solid material, while the remaining pixels were interpreted as pore space. This includes both open pores and resin-filled pores, which are treated equivalently for the purpose of analysis. The porosity was then calculated as the ratio of pore pixels to the total number of pixels representing both dense material and pores. Although this analysis is strictly limited to a two-dimensional cross-section, it is assumed that the results are representative of the specimens' volumetric porosity.

The pressure in the vacuum chamber was measured every second with a pressure gauge (Pirani gauge PPT 200, Pfeiffer Vacuum GmbH). For scanning electron microscopy (SEM) imaging of the powders, a Quanta FEG 400 ESEM (FEI Company) was used. The same instrument using an Everhart Thornley Detector was employed for energy-dispersive X-ray spectroscopy (EDX) analysis, which was conducted using the EDAX APEX Advanced software version 3.0 (AMETEK GmbH).

3. Results and Discussion

3.1. Drying state

Following the drying process, a distinct color change was observed in the simulant powder. Initially beige, the powder darkens when dried at 300 °C and develops a brown coloration at 800 °C. This change, illustrated in Figure 3, suggests the

occurrence of oxidation during thermal treatment. The color change is most noticeable in the iron-rich TUBS-M simulant, which supports the assumption of oxidation.

To verify that the drying process does not significantly alter the chemical composition or morphology of the particles, SEM and EDX analyses were conducted. The SEM images (Appendix A.) reveal no notable morphological changes; the particles remain sharp-edged and continue to display a broad particle size distribution. The EDX analysis (see Appendix B. shows that all elements present in the simulant powder before drying (see Table 1) were still present after the drying process. Based on the analysis, no conclusions can be drawn regarding changes in the elemental distribution. However, the distribution of the peaks remains similar across the three measurements. Further investigations using more sensitive or complementary analytical techniques may be required to fully assess potential chemical modifications or oxidation states.

Figure 3 also shows the results of the melting process. Experiments using undried powder did not produce cohesive specimens. Only isolated, non-connected melt beads were formed, which is why these specimens were not further analyzed. The process was highly irregular, as indicated by the spatters and unmelted particles scattered across the specimen and the powder tray. Although the image of the undried TUBS-T specimen is missing, the experiment was conducted with similar outcomes.

When laser melting the simulant dried at 300 °C, noticeably less spattering occurred, and partially cohesive specimens could be produced. Additionally, it appears that the specimens become wider with an increasing TUBS-M content, which corresponds to darker powders and higher laser absorption.

Laser melting of the powder dried at 800 °C resulted in a significantly more stable process and spattering was nearly eliminated. The resulting specimens were distinctly wider, clearly defined, and cohesive. The specimens made from TUBS-M exhibited a shiny, uniformly black surface, while those from TUBS-T and the South Pole simulant were notably brighter in color with more heterogeneous coloration. Morphologically, the TUBS-T and South Pole specimens also appeared less regular in shape compared to TUBS-M specimens.

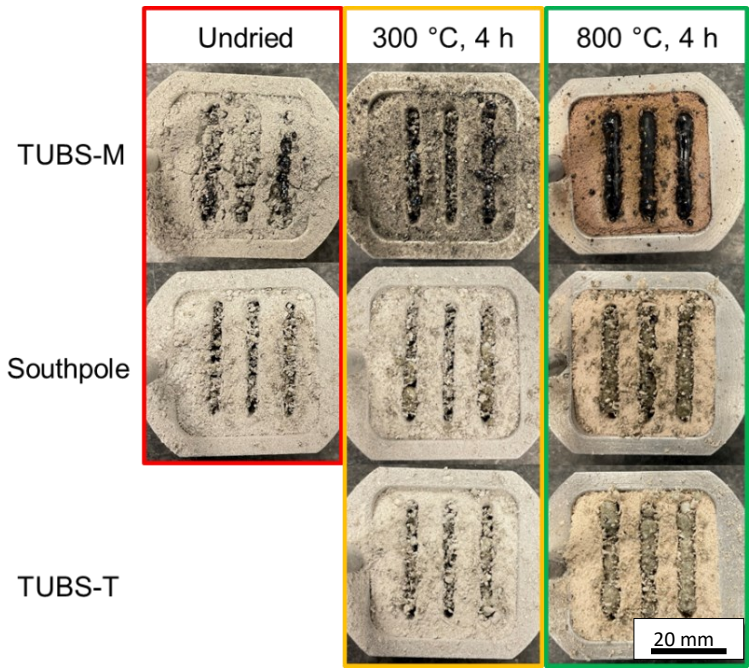

Figure 3. Powder beds dried at different temperatures with specimens inside

As previously mentioned, mass analysis was only conducted for specimens from drying states where at least three specimens could be fully extracted from the powder bed. This criterion was met for specimens produced from powder dried at 800 °C and from the South Pole simulant dried at 300 °C.

The results of the mass analysis are presented in Figure 4. The data show that specimens produced from the South Pole simulant dried at 300 °C exhibited lower average masses compared to those made from powder dried at 800 °C. This trend corresponds well with the geometric dimensions of the specimens shown in Figure 3. Furthermore, an increase in specimen mass is observed with rising TUBS-M content—i.e., as the powder becomes darker. This is consistent with the higher laser absorption expected for the darker TUBS-M simulant relative to the brighter TUBS-T.

The highest average specimen mass was obtained from TUBS-M specimens produced using powder dried at 800 °C, reaching approximately 950 mg. The South Pole simulant dried at 800 °C yielded specimens with an average mass of about 750 mg, while specimens made from TUBS-T dried at 800 °C had an average mass of approximately 650 mg. In contrast, the South Pole simulant dried at 300 °C yielded the lowest average specimen mass, around 450 mg, which is roughly half of the TUBS-M specimens produced from powder dried at 800 °C.

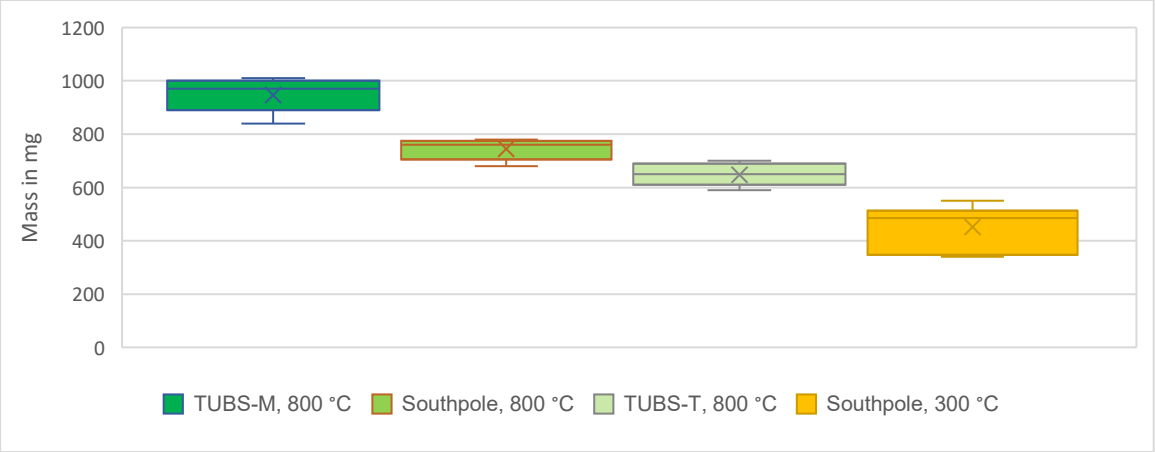

Figure 4. Mass of specimens from different simulants dried at 300 °C and 800 °C

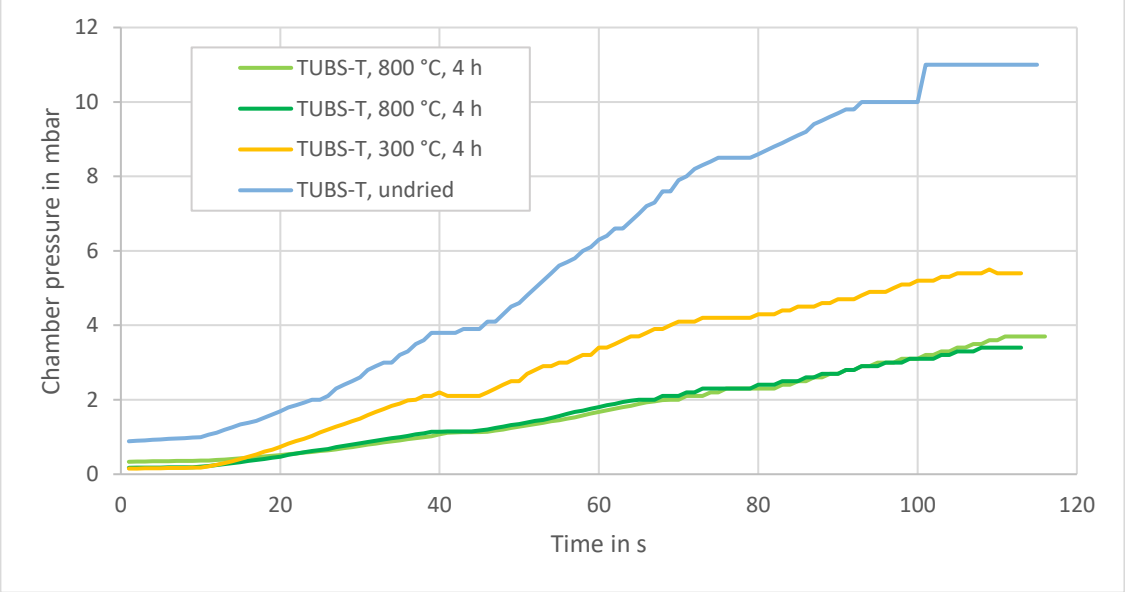

Figure 5. Increase in chamber pressure during laser melting of TUBS-T simulant. The two green lines correspond to two individual runs.

The pressure increase in dependence of the drying state shows a similar trend across all simulant types. Figure 5 illustrates the pressure profiles for the different drying states of TUBS-T. The plateaus at approximately 40 seconds and 75 seconds occur because the laser is switched off while it is being moved to the start of the next specimen. It is evident that the lowest pressure rise occurs for powder dried at 800 °C, for which the pressure increases steadily to approximately 3.4 to 3.7 mbar.

For the TUBS-T powder dried at 300 °C, the pressure rise is slightly higher, peaking at approximately 5.5 mbar. By far the highest pressure increase is observed for the undried powder, for which the pressure reaches approximately 10 mbar. In addition, the pressure curve for the undried powder is highly irregular, and the initial target pressure could not be reached. In this case, the process started at approximately 1 mbar, instead of 1.5×10^{-2} mbar.

Representative cross-sectional images of selected specimens are provided in Figure 6 and Figure 7 (a). As shown in Figure 7 (a), specimens fabricated from TUBS-M simulant dried at 300 °C exhibit significantly reduced thickness compared to those

produced from simulant dried at 800 °C, as shown in Figure 6. This observation is consistent with the mass data previously discussed.

In several cases, particularly for specimens produced from both 300 °C and 800 °C dried TUBS-M simulant, straight lateral edges are observed on the left side of the cross-sections. This feature is indicative of direct contact between the specimens and the bottom of the powder tray, suggesting substantial sinking into the powder bed during the process. Such contact introduces additional thermal conduction pathways and effectively renders the tray a local heatsink, thereby influencing melt pool dynamics and solidification behavior.

Among the specimens derived from powders dried at 800 °C, a clear trend emerges. An increasing TUBS-M content corresponds to darker powder coloration and higher absorptivity, which leads to thicker and overall, more voluminous specimens. This trend aligns with the previously observed increase in specimen mass as a function of TUBS-M fraction.

In terms of porosity, no systematic differences could be discerned qualitatively from the cross-sectional images. Two distinct pore types were identified and considered equally in the analysis. On the one hand, resin-filled pores, which exhibit similar contrast to the matrix are present. On the other hand, unfilled voids, appearing as dark inclusions can be observed. Due to the limited number of fully analyzable cross-sections, quantitative porosity measurements could only be performed on a small subset of specimens. These results are summarized in Figure 7 (b).

The measured porosities range between 62% and 73%, which is consistent with values reported in the literature for unidirectionally melted geometries produced under comparable conditions (Eismann et al. 2023). Although the dataset does not support statistically robust conclusions, it is reasonable to assume that the porosity of all specimens lies within this range.

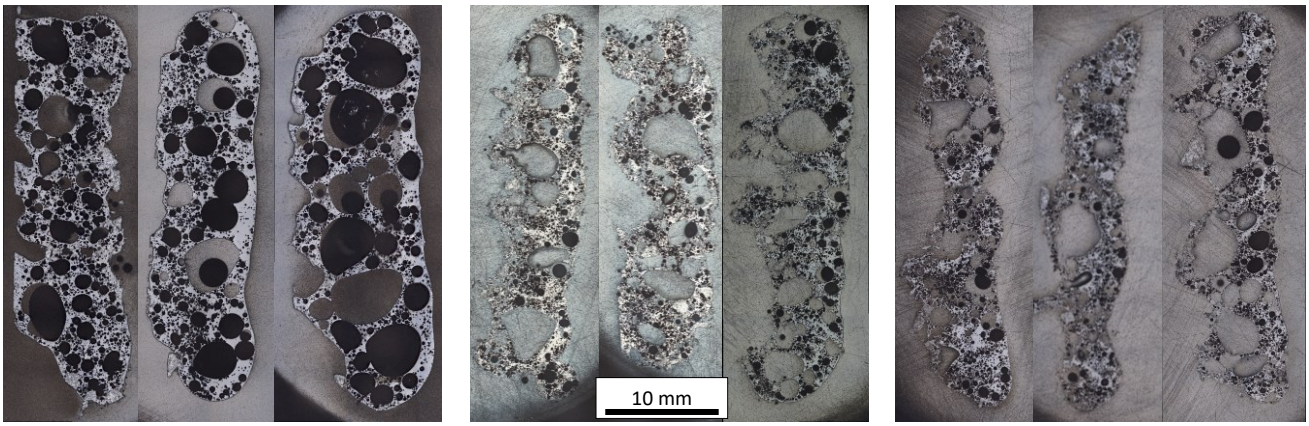

Figure 6. Cross sections of specimens manufactured from powders dried at 800 °C from (a) TUBS-M, (b) South Pole simulant and (c) TUBS-T

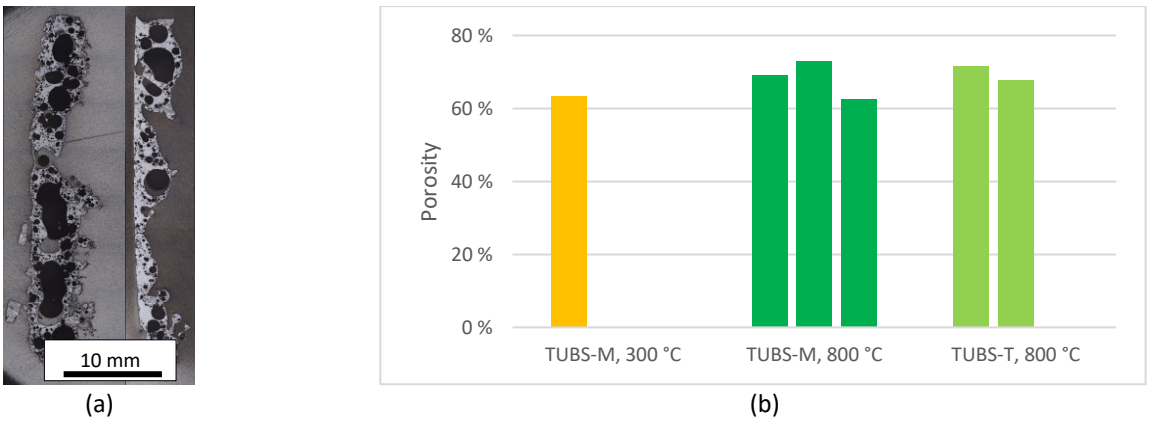

Figure 7. (a) Cross section of specimens manufactured from TUBS-M dried at 300 °C and (b) Result of porosity analysis for individual specimens (one bar corresponds to one specimen)

3.2. Particle size distribution

Figure 8 shows that cohesive specimens could be successfully produced using all three PSDs. Qualitatively, the specimens appear to become narrower as the particle size decreases.

The specimens fabricated from particles in the 500 – 1000 µm range are uniform and exhibit a nearly constant width along their entire length. Some powder particles are partially sintered onto the specimens and could not be removed with a brush. Additionally, the surrounding powder bed shows a brown discoloration, likely due to oxidation.

The specimens produced from the 160 – 250 µm PSD are slightly less uniform than those made with the coarser particles. Fewer particles are fused to the specimen surface. Brown discoloration is also present in the powder bed, but its intensity varies, being darker near the specimen and lighter toward the edges.

Specimens produced from the < 90 µm PSD are visibly narrower and exhibit spherical formations on the top surface, which could be related to the balling effect known from PBF-LB/M. In these specimens, the brown discoloration is homogeneously distributed across the entire powder bed. It is hypothesized that the increased thermal conductivity of the fine powder allows for greater heat dissipation, leading to oxidation over a wider area of the powder bed surface.

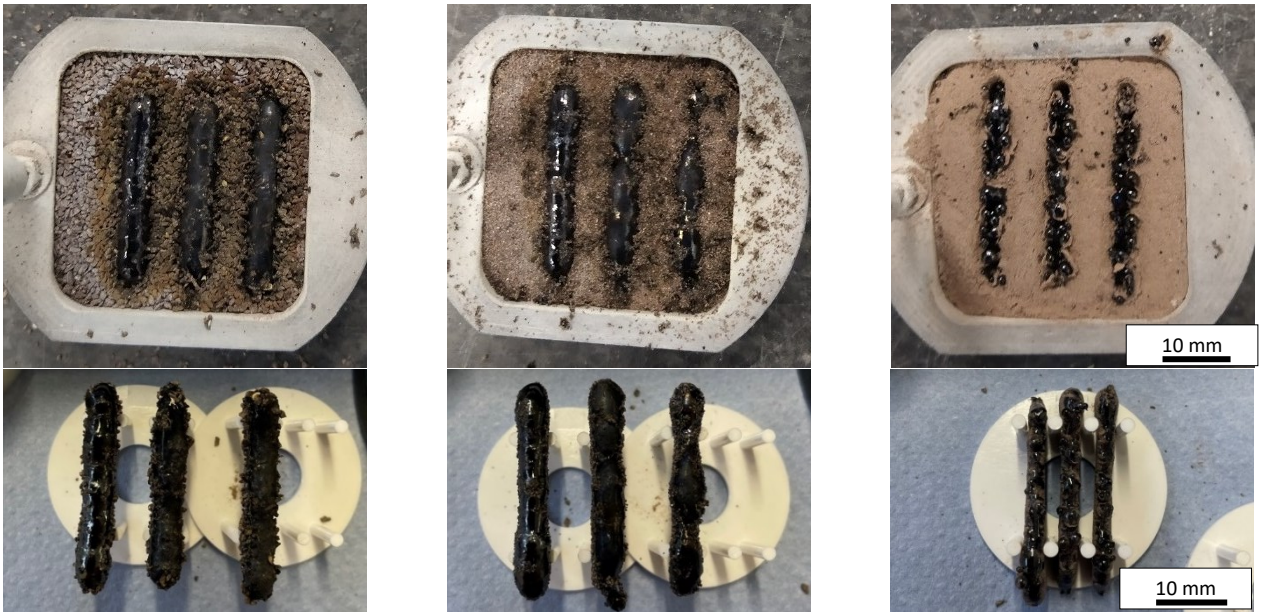

Figure 8. Specimens from TUBS-T in different PSDs. (a) 500 - 1000 µm, (b) 160 - 250 µm, (c) < 90 µm

The pressure increase in the vacuum chamber during the melting of the simulants is shown in Figure 9. The lowest pressure increase was observed in the experiments using particles with a size range of 160 – 250 µm, averaging approximately 0.5 mbar per specimen. A slightly higher increase of around 0.55 mbar was recorded for the 500 – 1000 µm fraction, although this difference is not considered significant.

In contrast, a notably higher pressure increase of approximately 0.7 mbar per specimen was observed with the < 90 µm particle size fraction. This is presumed to result from the evaporation of finer particles, which have a higher surface area-to-volume ratio and are more susceptible to thermal degradation and vaporization under the given process conditions.

Notably, the pressure increase observed in all cases in this experiment is approximately half of that measured in the previous study using TUBS-T simulant dried at 800 °C, where values between 3.4 and 3.7 mbar were recorded (see Figure 5). The reason for this discrepancy remains unclear. One possible explanation could be a higher leakage rate of the vacuum chamber during the earlier experiments. Nonetheless, this behavior should be further investigated to clarify the underlying cause.

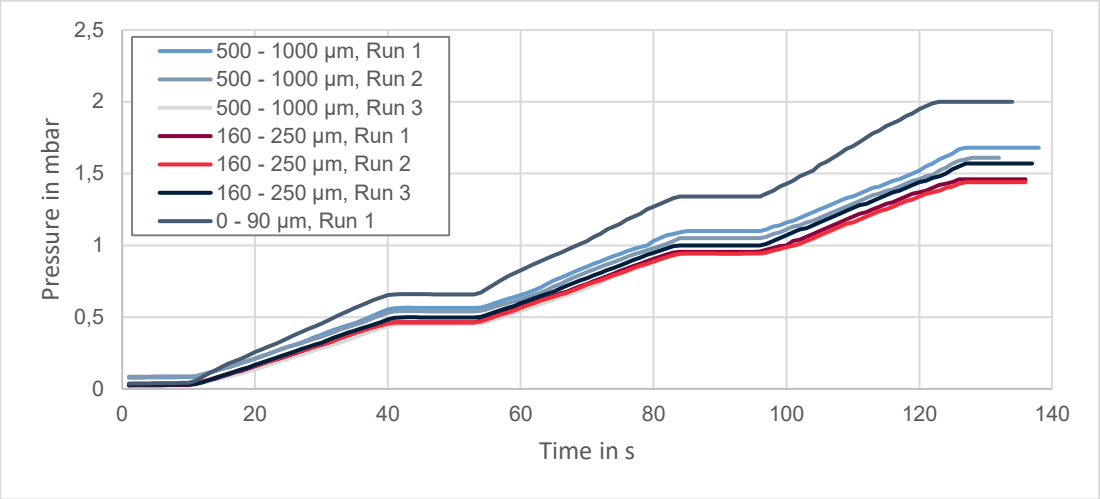

Figure 9. Increase in chamber pressure during laser melting of TUBS-T simulant. Each curve consists of 3 slopes and each slope represents the melting of one specimen.

The width and length of the specimens, as viewed from above, are presented in Figure 10. The specimens produced from the 500 – 1000 µm and 160 – 250 µm particle size fractions exhibit approximately the same average dimensions. They are about 31 mm in length, which corresponds to the sum of scan vector length and laser spot diameter, and on average 4.6 mm in width. The specimens made from the 160 – 250 µm fraction show a greater variation in width, which may be attributed to their less uniform shape. In contrast, the specimens made from the < 90 µm fraction are only about 26 mm long and approximately half as wide as the others.

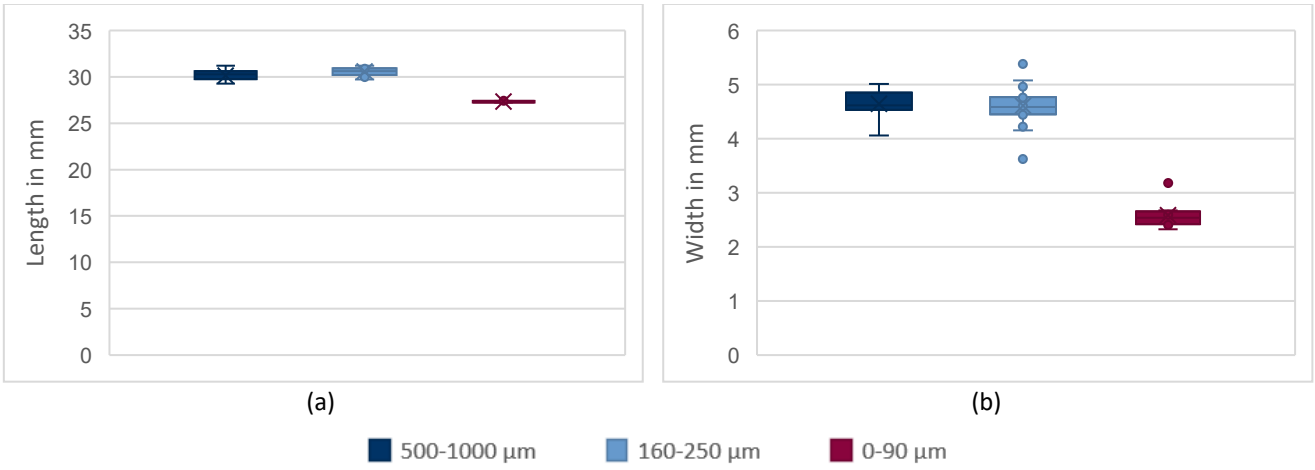

Figure 10. Length and width of specimens laser beam molten from TUBS-T simulant

Figure 11 (a) shows the specimen mass grouped by PSD. As expected based on their dimensions, the specimens from the < 90 µm fraction have the lowest average mass of approximately 0.59 g. This is followed by the 160 – 250 µm fraction with an average of around 0.79 g. The specimens from the 500 – 1000 µm fraction exhibit the highest mass, with an average mass of 0.89 g, despite having the same geometric dimensions as those made from the 160 – 250 µm fraction.

This difference may be due to partially sintered particles on the specimen surface that were not accounted for during geometric measurements, deeper penetration into the powder bed, or a lower specimen porosity.

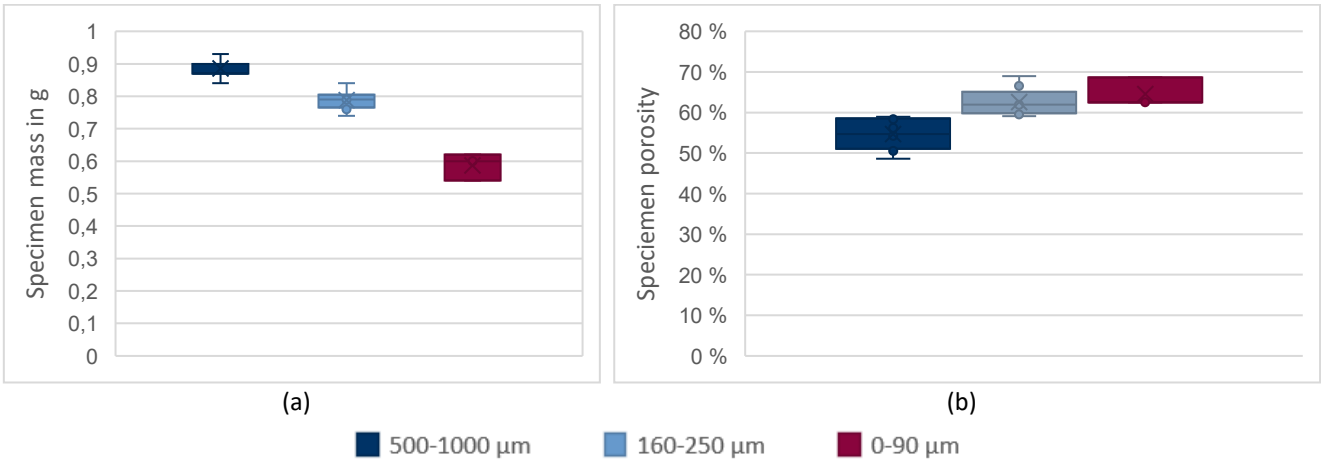

Figure 11. Mass and porosity of specimens laser beam molten from TUBS-T simulant

Figure 11 (b) shows that the specimens made from the 500 – 1000 µm fraction exhibit a lower porosity of approximately 55%, compared to about 63% for the 160 – 250 µm fraction and around 65% for the 0 – 90 µm fraction.

The cross-sectional images of the specimens, shown in Figure 12 (a), reveal that the 500 – 1000 µm specimens contain noticeably fewer pores. These pores are mostly spherical, with diameters not exceeding 4 mm, and are smaller in size compared to those observed in the other fractions. The specimens also appear relatively uniform in the third spatial direction, which had not been observed previously.

In contrast, the specimens made from the 160 – 250 µm fraction exhibit a slightly wavy shape and appear thicker. The pores are larger and, in some cases, interconnected, a characteristic also observed in specimens made of powder with a particle diameter < 90 µm.

The cross-sections of the specimens manufactured from the < 90 µm PSD show an irregular top surface, shaped by the balling effect. The bottom surface, however, is flat, indicating that the specimens sank deep enough into the powder bed to contact the bottom of the powder tray. This contact likely caused the powder bed tray to act as a heat sink, thereby influencing the process. In the contact area, the specimens exhibit a lower porosity.

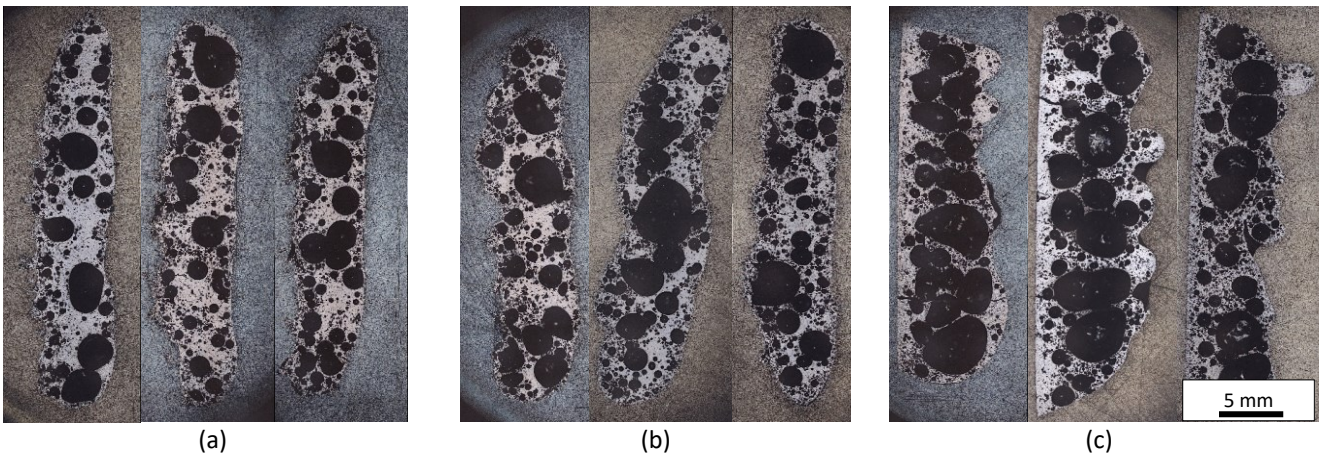

Figure 12. Cross section of specimens from TUBS-T simulant with (a) 500 - 1000 µm PSD, (b) 160 - 250 µm and (c) < 90 µm

4. Conclusion

The results clearly demonstrate that the drying state significantly affects the processability of the regolith simulant. Untreated powder is almost unprocessable, producing no cohesive specimens and exhibiting a highly unstable melting behavior. Drying at 300 °C leads to partial improvements, allowing the formation of some cohesive structures, but the process remains irregular. Stable and reproducible processing is only achieved after drying at 800 °C. This high-temperature treatment is expected to remove both residual moisture and water of crystallization from the powder and is proven essential

for achieving a controlled and continuous melting process. While SEM and EDX analyses did not reveal measurable changes in particle morphology or chemical composition, a visible discoloration of the powder from beige to brown indicates oxidation during drying.

While none of the PSDs were found to be fundamentally limiting, finer particles (< 90 µm) were associated with less uniform specimen geometries, increased oxidation, and signs of process instabilities such as the balling effect. These observations suggest that coarser powders are more favorable for the specific processing conditions applied in this study.

Several phenomena observed during the experiments reveal the need for further investigation. The origin and implications of this color change will be systematically investigated to better understand potential oxidation processes during thermal treatment. To eliminate the influence of atmospheric oxygen, drying experiments under vacuum conditions are planned. Additionally, the origin of the observed pressure increase during the melting process will be studied using a mass spectrometer connected to the build chamber to analyze the elemental composition of the released gases. To ensure that thermal behavior mimics lunar conditions more closely, future experiments will employ a larger powder bed. The influence of the powder bed dimensions and the thermal properties of the powder tray will be evaluated with the aim of minimizing unintended heat conduction effects. These next steps shall contribute to a refined process understanding and enable a more robust additive manufacturing with simulant materials under controlled atmospheric conditions.

Acknowledgements

Funded by Space Agency of the German Aerospace Center (DLR) with federal funds of the Federal Ministry for Economic Affairs and Energy in accordance with a parliamentary resolution of the German Parliament (grant no. 50WP2206A and 50WP2206B).

Federal Ministry
for Economic Affairs
and Climate Action

References

Averardi, Alessandro; Cola, Corrado; Zeltmann, Steven Eric; Gupta, Nikhil (2020): Effect of particle size distribution on the packing of powder beds: A critical discussion relevant to additive manufacturing. In *Materials Today Communications* 24, p. 100964. DOI: 10.1016/j.mtcomm.2020.100964.

Caprio, Leonardo; Demir, Ali Gökhan; Previtali, Barbara; Colosimo, Bianca Maria (2020): Determining the feasible conditions for processing lunar regolith simulant via laser powder bed fusion. In *Additive Manufacturing* 32, p. 101029. DOI: 10.1016/j.addma.2019.101029.

Eismann, T.; Griemsmann, T.; Schroeder, C.; Emminghaus, N.; Weßels, P.; Neumann, J. et al. (2024): Laser remelting of regolith in vacuum: Reducing porosity for enhanced lunar resource utilization. In *Procedia CIRP* 124, pp. 494–498. DOI: 10.1016/j.procir.2024.08.160.

Eismann, Tim; Griemsmann, T.; Ernst, M.; Taschner, P.; Dyroey, P.; Kalms, R. et al. (2023): Entwicklung von Prozessparametereinstellungen für das Laserstrahlschmelzen von Regolith unter Vakuum. DOI: 10.21268/20230711-10.

Fateri, Miranda; Gebhardt, Andreas (2015): Process Parameters Development of Selective Laser Melting of Lunar Regolith for On-Site Manufacturing Applications. In *Int. J. Appl. Ceram. Technol.* 12 (1), pp. 46–52. DOI: 10.1111/ijac.12326.

Fateri, Miranda; Gebhardt, Andreas; Khosravi, Maziar (2013): Experimental Investigation of Selective Laser Melting of Lunar Regolith for In-Situ Applications. DOI: 10.1115/IMECE2013-64334.

Gerdes, N.; Fokken, L. G.; Linke, S.; Kaierle, S.; Suttmann, O.; Hermsdorf, J. et al. (2018): Selective Laser Melting for processing of regolith in support of a lunar base. In *Journal of Laser Applications* 30 (3), p. 32018. DOI: 10.2351/1.5018576.

Griemsmann, Tjorben; Ernst, Mathias; Perwas, Jan; Eismann, Tim; Kalms, Roland; Emminghaus, Nicole et al. (2024): Single-Layer Laser-Based Powder Bed Fusion of Lunar Regolith Simulants in Vacuum as a First Step to Direct Additive Manufacturing on the Moon. DOI: 10.58134/FH-AACHEN-RTE_2024_013.

Griemsmann, Tjorben; Patzwald, Joel; Chawda, Chetan; Eismann, Tim; Abel, Arvid; Emminghaus, Nicole et al. (2025): Influence of ambient pressure on laser beam melting of lunar regolith simulant. In *Acta Astronautica* 228, pp. 30–41. DOI: 10.1016/j.actaastro.2024.11.057.

Gusarov, A. V.; Kovalev, E. P. (2009): Model of thermal conductivity in powder beds. In *Phys. Rev. B* 80 (2). DOI: 10.1103/physrevb.80.024202.

Heiken, Grant H.; Vaniman, David T.; French, Bevan M. (1991): Lunar Sourcebook, A User's Guide to the Moon. In *Lunar Sourcebook, A User's Guide to the Moon*.

Isachenkov, Maxim; Chugunov, Svyatoslav; Akhatov, Iskander; Shishkovsky, Igor (2021): Regolith-based additive manufacturing for sustainable development of lunar infrastructure – An overview. In *Acta Astronautica* 180, pp. 650–678. DOI: 10.1016/j.actaastro.2021.01.005.

Jolliff, Bradley L.; Neal, Clive R.; Shearer, Charles K.; Wieczorek, Mark A. (Eds.) (2006): New Views of the Moon. Berlin, Boston: De Gruyter (Reviews in Mineralogy & Geochemistry, 60).

Krishna Balla, Vamsi; Roberson, Luke B.; O'Connor, Gregory W.; Trigwell, Steven; Bose, Susmita; Bandyopadhyay, Amit (2012): First demonstration on direct laser fabrication of lunar regolith parts. In *Rapid Prototyping Journal* 18 (6), pp. 451–457. DOI: 10.1108/13552541211271992.

Linke, Stefan (2022): Mechanische Werkstoffeigenschaften von lasergeschmolzenem lunaren Regolith. With assistance of Enrico Stoll, Carsten Schilde. Braunschweig: Technische Universität Braunschweig.

Linke, Stefan; Windisch, Lisa; Kueter, Nico; Wanvik, Jan Egil; Voss, Anna; Stoll, Enrico et al. (2020): TUBS-M and TUBS-T based modular Regolith Simulant System for the support of lunar ISRU activities. In *Planetary and Space Science* 180, p. 104747. DOI: 10.1016/j.pss.2019.104747.

Neumann, J.; Ernst, M.; Taschner, P.; Perwas, J.; Kalms, R.; Griemsmann, T. et al. (2023): The MOONRISE-payload as proof of principle for mobile selective laser melting of lunar regolith, p. 230. DOI: 10.1117/12.2691126.

Overmeyer, Ludger; Raupert, Marvin; Pusch, Matthias; Griemsmann, Tjorben; Katterfeld, André; Lotz, Christoph (2025): Laser powder directed energy deposition and substrate-free single layer powder bed fusion under micro- and lunar gravity conditions. In *CIRP Annals* 74 (1), pp. 297–301. DOI: 10.1016/j.cirp.2025.03.031.

Popovich, Vera; Laot, Mathilde; Cheibas, Ina; Rich, Belinda (2020): Additive manufacturing of functionally graded materials from lunar regolith. Available online at https://nebula.esa.int/content/additive-manufacturing-functionally-graded-ceramics-situ-resources.

Reitz, B.; Lotz, C.; Gerdes, N.; Linke, S.; Olsen, E.; Pflieger, K. et al. (2021): Additive Manufacturing Under Lunar Gravity and Microgravity. In *Microgravity Sci. Technol.* 33 (2). DOI: 10.1007/s12217-021-09878-4.

Sacksteder, Kurt; Sanders, Gerald (2007): In-Situ Resource Utilization for Lunar and Mars Exploration. In : 45th AIAA Aerospace Sciences Meeting and Exhibit. 45th AIAA Aerospace Sciences Meeting and Exhibit. Reno, Nevada. Reston, Virigina: American Institute of Aeronautics and Astronautics.

Slabic, Ane; Gruener, John E.; Kovtun, Rostislav N.; Rickman, Douglas L.; Sibille, Laurent; Oravec, Heather A. et al. (2024): Lunar Regolith Simulant User's Guide: Revision A. National Aeronautics and Space Administration (NASA/TM-20240011783). Available online at https://ntrs.nasa.gov/citations/20240011783.

Zhang, Jiayao; Gu, Dongdong; Yang, Ying; Zhang, Hongmei; Chen, Hongyu; Dai, Donghuai; Lin, Kaijie (2019): Influence of Particle Size on Laser Absorption and Scanning Track Formation Mechanisms of Pure Tungsten Powder During Selective Laser Melting. In *Engineering* 5 (4), pp. 736–745. DOI: 10.1016/j.eng.2019.07.003.

Appendix A. SEM images from TUBS-T simulant powders

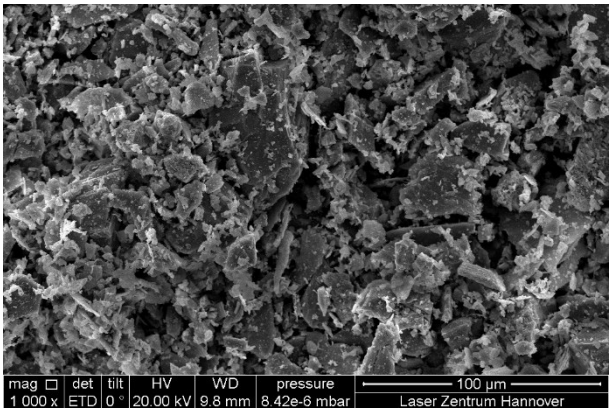

Figure 13. SEM image of undried TUBS-T simulant

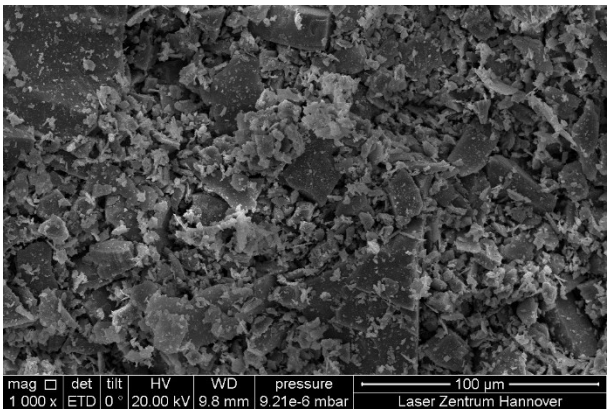

Figure 14. SEM image of TUBS-T simulant powder dried at 300 °C for 4 h under ambient atmosphere

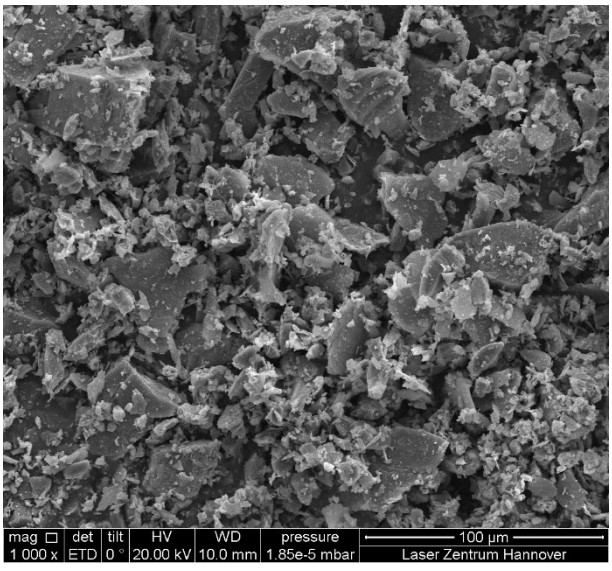

Figure 15. SEM image of TUBS-T simulant powder dried at 800 °C for 4 h under ambient atmosphere

Appendix B. EDX analysis of TUBS-T simulant powders

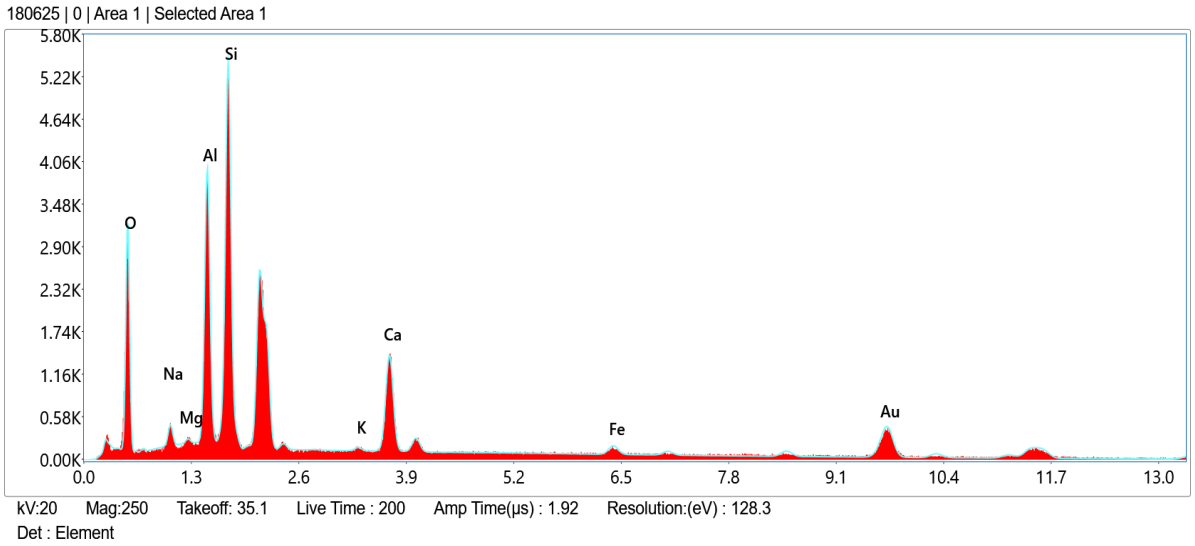

Figure 16. EDX analysis of undried TUBS-T simulant

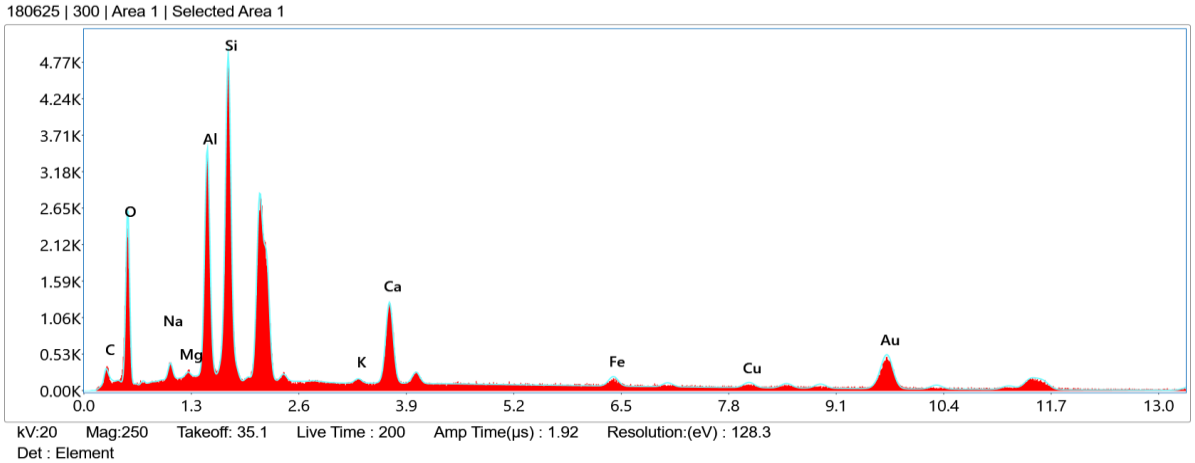

Figure 17. EDX analysis of TUBS-T simulant powder dried at 300 °C for 4 h under ambient atmosphere

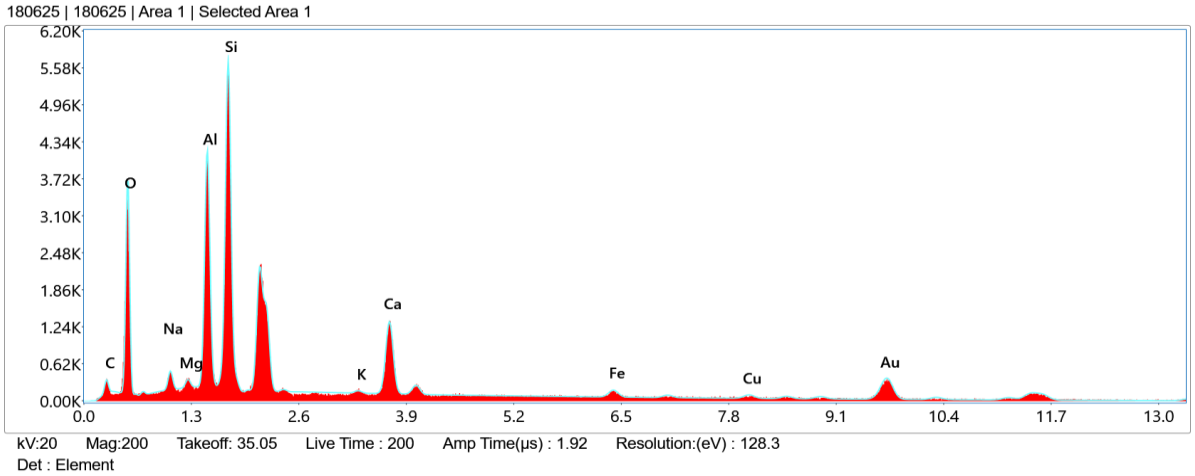

Figure 18. EDX analysis of TUBS-T simulant powder dried at 800 °C for 4 h under ambient atmosphere